IEEE Access
Multidisciplinary ⋮ Rapid Review ⋮ Open Access Journal

Received 23 February 2024, accepted 27 April 2024, date of publication 6 May 2024, date of current version 13 May 2024.

Digital Object Identifier 10.1109/ACCESS.2024.3397161

RESEARCH ARTICLE

Electric Field Distributions in Laser Drilled Voids of Polymeric Test Samples

YUE XU[1], (Member, IEEE), KENT DAVEY[1], (Life Fellow, IEEE), WENPING ZHAO[2], ROBERT E. HEBNER[1], (Life Fellow, IEEE), AND MIAD YAZDANI[2]

[1]Center for Electromechanics, The University of Texas at Austin, Austin, TX 78758, USA
[2]Raytheon Technologies Research Center, East Hartford, CT 06108, USA

Corresponding author: Yue Xu (y.xu@cem.utexas.edu)

This work was supported by the National Aeronautics and Space Administration under Contract NNC15BA06B.

ABSTRACT Future electric transportation systems are expected to employ electrical power trains with higher operating voltage and power density. Therefore, compact and reliable insulation systems are important, since they influence the system integration, thermal resistance, and parasitic inductance. In this paper, experiments and analysis show behavior which are not observed with mechanically produced holes before. A boundary element analysis of the electric field distribution around the voids reveals why these new observations are identified in voids with relatively sharp corners. The electric field computation shows conditions under which there is electric field enhancement at the void periphery. This drives the partial discharge (PD) activity and the erosion growth away from the center of the voids.

INDEX TERMS Boundary element electric field analysis, insulation aging and breakdown, partial discharge, tomography, White light interferometry.

I. INTRODUCTION

Electromechanical growth of voids in polymer insulation can be linked to Partial Discharge (PD) through gases released and thermal energy injected. Both compromise the useful life of the cable. To better understand these effects, three layers of the polymer are stacked as in Fig.1 with a laser drilled void through the center of the central layer. The void in the central layer encourages PD activity, and thus this experimental arrangement has been studied by many researchers [1], [2], [3], [4], [5].

Cable voids become the concern when they reach the size of a few micrometers. Voids used in earlier experimental studies of existing publications have diameters of a few thousand micrometers because they were drilled mechanically. Advances in laser drilling have made it possible to drill holes with diameters as small as 10 μm. At a macro level, the changes induced by PD in small cavities affect the electric field distribution, the gas pressure distribution, and the temperature in accordance with the governing gas law. Partial discharges deposit energy in the gas inside the voids, which raises temperature and gas pressure. Over time, each void returns to equilibrium with the ambient conditions via different diffusion processes. This investigation focuses on the effect of void size on the electric field distribution especially in or nearby the void region.

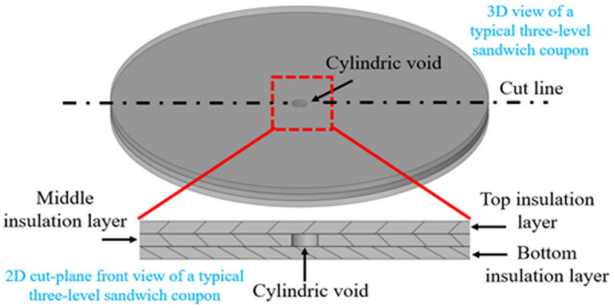

FIGURE 1. Typical accelerated aging test sample with an artificial void in the middle layer of the dielectric sample.

Transportation electrification provides the motivation for this study as it benefits from higher power density [6], [7]. Higher power density typically correlates with higher operating temperatures and often lower parasitic inductance.

The associate editor coordinating the review of this manuscript and approving it for publication was Youngjin Kim.

These conditions pose additional challenges to the design and integrity of the insulation system [8]. Future electric transportation systems will be characterized by smaller size and insulation weight, while providing a suitable basis for predicting system life. Thus, insulation design will play an increasing role in future electrified transportation systems [9].

II. EXPERIMENTAL APPROACH

The schematic for the experimental setup is shown in Fig.2. Two pictures taken from the front and side of the Faraday cage are shown in Fig.3. The line frequency (60 Hz) sinusoidal excitation is used throughout the various tests. For PD testing, a high frequency current transformer (HFCT) or a standard measurement impedance can be applied to convert the PD impulse current to a measurable pulse signal. A C-L-3C filter removes PD-like noise from the power supply. This setup supports ac PD tests up to 24 kV with background noise lower than 10 pC. The experiments are performed in a cylindrical stainless-steel tank, which is approximately 3 meters long and 1 meter in diameter. At atmospheric pressure, this test chamber is PD free up to ∼20 kV rms.

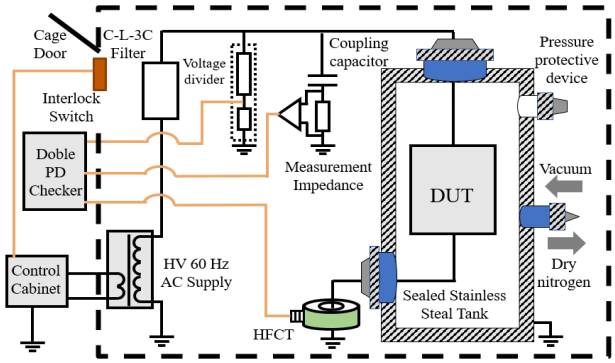

FIGURE 2. Schematic for the long-term PD aging test setup with minimally attended.

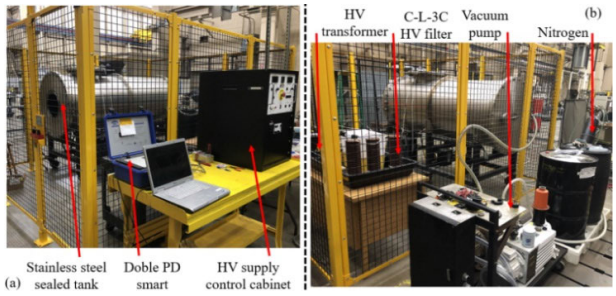

FIGURE 3. Long-term aging setup pictures: (a) Front view, (b) Side view.

Three layers of polymer sheets (perfluoroalkoxy alkane, PFA) are stacked in the test fixture as shown in Fig.4 (a). The thickness of each layer is 0.79 mm. The central layer contains one or more cylindrical voids (vertical axis) while the top and bottom polymer layers are nominally void-free. The polymer sheets are 85 mm long by 85 mm wide. An oil-filled transparent plastic cup is epoxied to the top surface of the test sample to eliminate surface discharges along the high voltage (HV) electrode edges. This simplifies the quantification of PD charge and PD energy since all PD events should only occur in the internal voids of the test sample.

The location of the electrodes (along vertical axis) can be adjusted via the threaded brass rods and thus mechanical force can be applied vertically to the three PFA layers. This can improve the contact between adjacent PFA sheets and reduce the contact resistance. The ground (GND) electrode diameter is 75 mm and the HV electrode diameter is 25 mm. The electrodes have rounded edges with a radius of 2.5 mm. The structure and various components in use are shown in Fig.4(b).

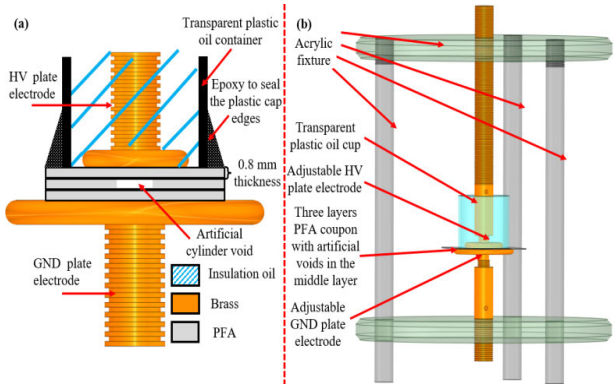

FIGURE 4. PFA accelerated aging test setup with internal PD: (a) An artificial void test sample with parallel plate electrodes. (b) Adjustable test fixture to hold the three-layer PFA test sample between two electrodes.

III. ANALYTICAL APPROACH

As stated in the introduction, a high precision boundary element analysis of the electric field distribution within the void can reveal the key information necessary to understand where PD activity would be greatest along the void periphery. The boundary element analysis shows how the electric field distribution varies depending on the size of the void and the sharpness of the void ceiling or floor corners. A summary of the numerical equations applied behind this method is presented in Appendix A.

IV. CONFOUNDING EFFECT OF LIQUID PRODUCTION

According to the [10], sustained PD produces liquid in three-layer test artifacts. For polypropylene (PP), the liquids are compounds, like formic, acetic, and carboxylic acids. If any one of the key constituents H, C or O is absent from the gas in the void, no liquid is produced.

In this investigation, analogous behavior was observed in three-layer PFA samples as shown in Fig.5 (a). Thermo-gravimetric (TGA) testing showed that prior to the PD testing, there were no volatile compounds like water trapped on the PFA material (Fig.5 (b)). It is probable that H, C and O in the air of the void lead to liquid formation.

Published research shows that the liquid modifies the surface and increases the surface conductivity of the void, which may affect the breakdown process [11], [12]. The

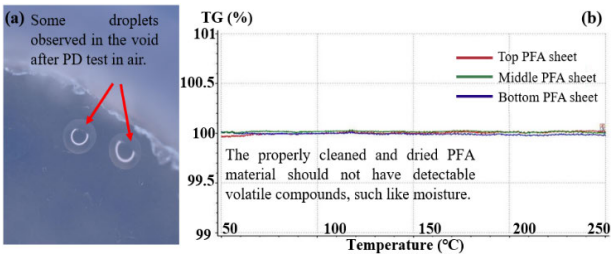

FIGURE 5. (a) Micrograph of droplets on the PFA surface in the void following extended PD testing in air (b) Tests show no volatile compounds are released from the PFA sheets over the range from 50 °C to 250 °C before the PD test.

presence of the liquid also may affect the electric field distribution. In this study, the effect was eliminated by conducting experiments in dry nitrogen rather than room air. It is a topic that warrants further investigation.

Fourier transform infrared spectroscopy (FTIR) analysis has been applied to PD-aged PFA samples, tested under dry nitrogen. A typical result is shown in Fig.6. No significant differences can be observed between FTIR spectra of baseline material (unaged PFA material in the same sheet) and the PD aged material with the 150 μm diameter void. This result further indicates that no unexpected chemical reactions are occurring during the accelerated PD aging of the PFA material in the dry nitrogen test condition.

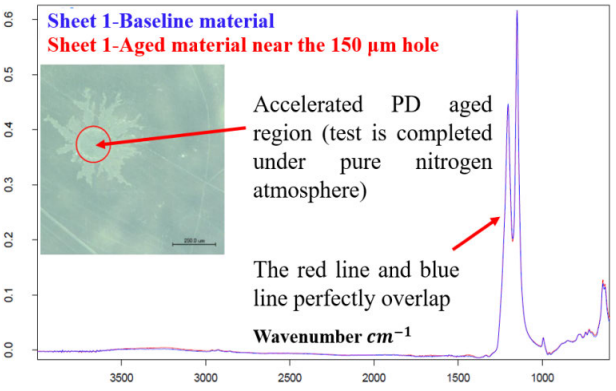

FIGURE 6. FTIR spectra comparison between the baseline material (unaged PFA material) and PD aged PFA material (tested under pure nitrogen) with the 150 μm diameter void.

V. ELECTRIC FIELD SIMULATION RESULTS

In this section, multiple simulation cases have been conducted in order to understand how the electric field (E-field) distribution in the void can be influenced by the geometrical parameters of the test samples and the relative permittivity of the selected insulation material. All the simulation cases can be divided into four categories, which will be mentioned as Case 1, Case 2, Case 3 and Case 4 in the following part. The major parameters of these 4 categories can be found in Table 1 and the difference among these simulation cases can also be identified there.

Five different situations are analyzed to provide insight into the electric field distributions that can occur within a void.

TABLE 1. Major geometrical parameters of the test samples and the relative permittivity of the selected insulation material applied in different simulation categories.

	Insulation Material Relative Permittivity	Void Diameter (µm)	Top and Bottom Layer Thickness (µm)	Middle Layer Thickness (µm)	Void Corner Radius (µm)
Case 1	2.06	2000	800	800	A
Case 2	4	2000	800	800	B
Case 3	2.06	100	X	X	Fixed
Case 4	2.06	100	Y	800	Fixed

* A, B, X and Y are variables which mean parameter sweepings are applied for that simulation case and geometrical dimension as indicated in the table.

**The same variable X occurs in two locations of Case 3 which means the values of those two geometrical dimensions are always the same during the parameter sweeping study.

Case 1 considers a 2000 μm diameter void, which is deemed representative of the large, mechanically produced voids in existing studies. Additionally, the electric field magnitude along the void periphery is further affected by the curvature of the void corner. For example, the void corner curvature affects PD initiation, which is influenced by the trapping of charges at the corner of the void ceiling. The geometry used in this simulation is shown in Fig.7 and results are reported in Fig. 8.

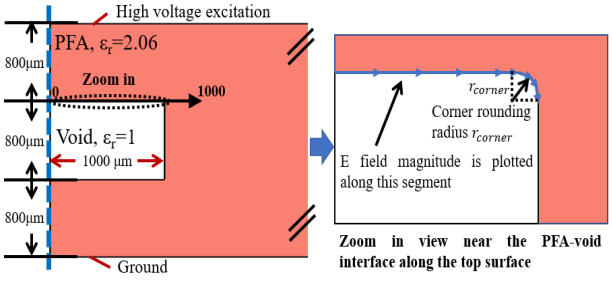

FIGURE 7. For a void of the 2000 μm diameter, the electric field is calculated along the void ceiling and plotted along the highlighted segment for various corner rounding radii. The voltage magnitude applied in this simulation is 12 kV rms under 60 Hz sinusoidal excitation.

Fig. 8 (a) and (b) show that before the corner rounding radius drops below 50 μm, the peak E-field will be at the center of the void. By comparison, when the corner rounding radius becomes smaller than 50 μm, the peak E-field will be at the corners. A smaller corner rounding radius will exhibit an even more intensified E-field magnitude along the corner than the center. Mechanical drilling or cutting produces relatively large corner radii, leading to minimal edge enhancement of the electric field.

In Fig.7, the relative permittivity is selected to be 2.06. Commonly used polymeric dielectrics, such as XLPE, PP, EPR, PVC, typically have permittivity ranging between 2 and 4. Thus, as shown in Fig.9, for the Case 2 simulations, after increasing the relative permittivity to 4, the peak electric field strength increases, but it has negligible influence on the electric field distribution in or near the void region. By comparing Fig.8 and Fig.9, a higher relative permittivity of the dielectric results in a larger E-field growth at the

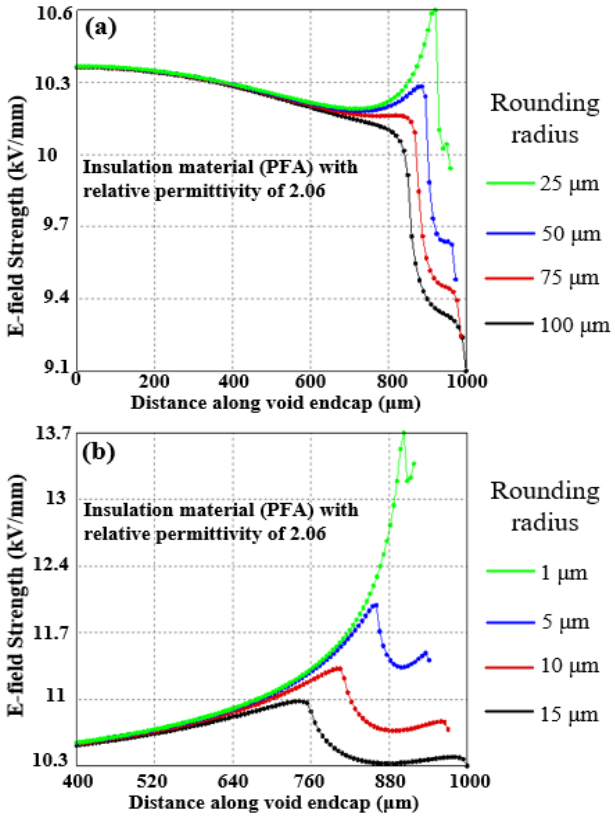

FIGURE 8. Case 1 simulations: the electric field distribution along the void ceiling as an example with the 2000 μm diameter, under various corner rounding radii, (a) 100 μm, 75 μm,50 μm, and 25μm and (b) 15μm, 10μm, 5 μm, and 1 μm.

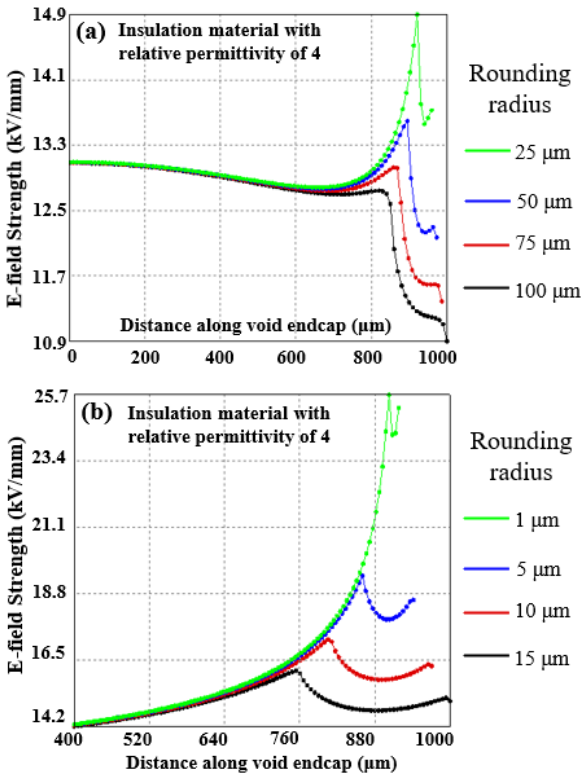

FIGURE 9. Case 2 simulations: if a polymer material with relative permittivity of 4 is applied instead of the PFA, the electric field distribution along the void ceiling of 2000 μm diameter with various corner rounding radii follows (a) 100 μm, 75 μm, 50 μm, and 25μm (b) 15 μm, 10 μm, 5 μm, and 1 μm.

corners. The difference between the E-field magnitude near the corner and the void center increases more than 3 times as the relative permittivity of the polymer material in use is doubled.

By varying the corner rounding radius, the same trend can be observed for small voids with a diameter less than 1 mm. For voids with diameters ranging from 100 μm to 800 μm, the electric field at the corner along the void periphery becomes dominant as the rounding radius is reduced. As a general conclusion for voids with a diameter less than 1000 μm, if the corner radius is less than 5% of the void diameter, the electric field along the corner for the void is larger than that near the center of the void. Two examples from simulations can be found in Fig.10, with void diameters ranging from 100 μm to 800 μm. The first set of curves maintains a corner rounding radius of 5 μm. The second set of void diameter curves repeats the analysis using a fixed corner rounding radius of 40 μm (5% of 800 μm). With the larger 40 μm rounding radius, it is clear that the E-field strength peaks start to move from the void corner to the void center, as the void diameters become smaller and smaller.

To match the experiments in the later sections, more simulation cases are studied with void diameters in the range between 10 μm and 500 μm. Since the E-field distribution is similar, only the results under void diameter of 100 μm will be presented in Case 3 and Case 4. The void corner radius used in the simulations for these cases is fixed to 5 μm.

Case 3 investigates the effect of the PFA layer thickness for all layers with the same thickness. The electric field intensity along the PFA layer thickness direction is fixed at 5 kV/mm in all simulations. With each PFA layer thickness of 200 μm, 400 μm, 600 μm and 800 μm, the simulation results are summarized in Fig.11. This analysis shows that for layer thicknesses are large compared to the void size, enhancement of the electric field at the void corner always occurs as predicted in Case 1.

Case 4 analyzes the situation for which the central layer is fixed at the thickness of 800 μm and the thickness of the top and bottom PFA layers are changed. Other simulation conditions are the same as those in Case 1. A typical electric field distribution is represented in Fig.12 with a 100 μm diameter void. The enhancement of the electric field at the void corner can be found in all simulations as shown in Fig.12.

VI. COMPARISON BETWEEN EXPERIMENT AND ANALYSIS

In order to verify the observations shown in the simulations above, typical three-layer accelerated PD aging test samples with laser drilled voids in the middle layer have been tested. Testing time is reduced by conducting tests of several voids

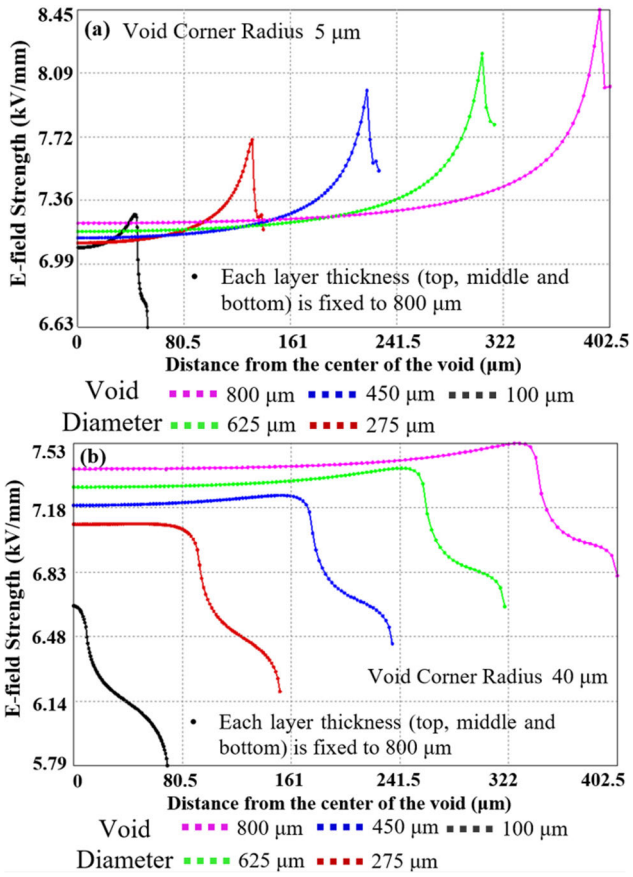

FIGURE 10. All insulation layer thickness is 800 μm with relative permittivity of 2.06 (a) E-field distribution under several different void diameters with fixed void rounding corner radius of 5 μm (b) E-field distribution under several different void diameters with fixed void rounding corner radius of 40 μm.

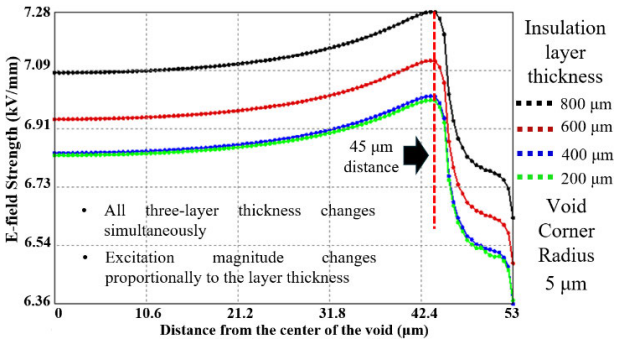

FIGURE 11. Case 3 simulations: Electric field distribution along the void ceiling with 100 μm void diameter, under various PFA thickness 800 μm, 600μm, 400 μm, and 200 μm.

in parallel. This is accomplished by designing a middle layer with multiple holes. The pattern used in the experiments has one hole of each 500 μm, 300 μm, 150 μm, 100 μm and 70 μm diameter, three holes with 30 μm diameter, and three holes with 10 μm diameter, as shown in Fig.13. The distance between adjacent holes is greater than 5 mm, while the shortest distance from a hole to the high voltage electrode

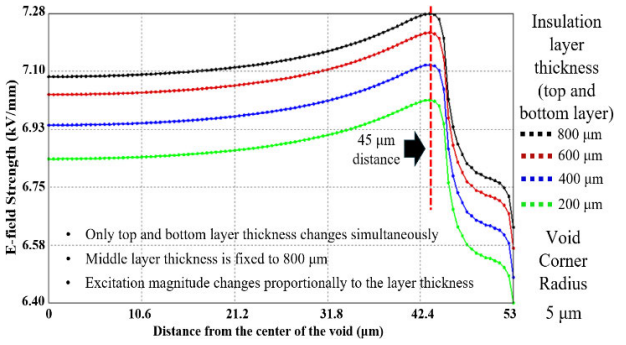

FIGURE 12. Case 4 simulations: Electric field distribution along the void ceiling with 100 μm void diameter, under various top and bottom PFA layer thickness 800 μm, 600 μm, 400 μm, and 200 μm, while the middle PFA layer thickness is fixed to 800 μm.

edges is about 6 mm. This design minimizes interactions between holes and electrode edge effects.

The laser-drilled polymer sheets (drilled by Potomac Photonics, Inc.) are prepared by cleaning with alcohol and deionized water, followed by drying at 105 ° for 4 hours to remove any moisture. After cleaning and drying, the quality of the holes and their nearby regions are inspected under the microscope. A typical picture is shown in Fig.14. The hole size is about 30 to 50 μm larger than specified. The hole shape is not perfectly circular, due to the laser drilling process, especially for the voids with smaller diameters.

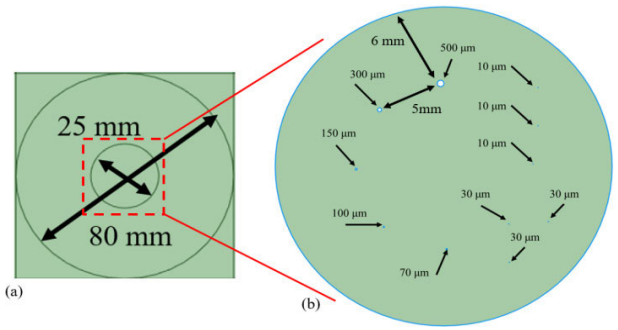

FIGURE 13. Laser drilled PFA proof sheet: (a) Top view of the 80 mm by 80 mm PFA sheet with all holes drilled in the center circular area of 25 mm diameter, (b) The zoom-in view of center area with 11 holes.

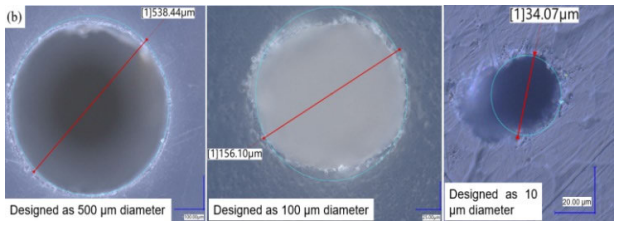

FIGURE 14. Received laser drilled PFA sheet under microscope check (the PFA sheets are properly cleaned and dried before checking).

The dominant factors which influence the E-field distribution in the simulations are the void size and the void corner radius. Small irregular shapes or differences in void diameter

will have a little effect on the E field magnitude in the corner. However, significant mismatches in shape and size require simulation modifications. This paper focuses on laser drilled holes with diameters bigger than 100 μm to help explain differences from prior similar work. Thus, some small void shape differences between the experiments and simulations will not influence the conclusions much here.

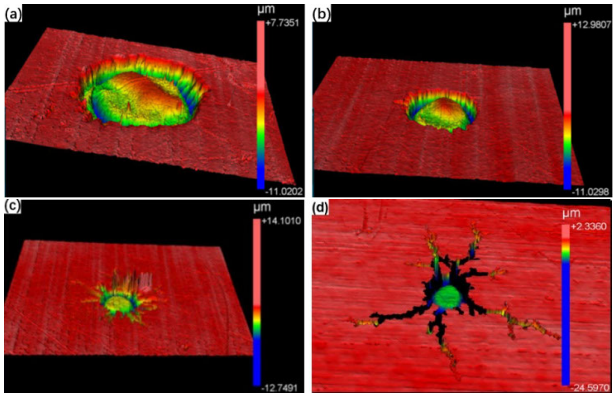

FIGURE 15. Erosion pattern from PD in the cylindrical void with nominal diameter (a) 500 μm (b) 300 μm (c) 150 μm (d) 100 μm.

Based on the simulation results provided in the previous sections of this paper, streamer initiation [13] in laser-drilled small voids should appear at the void periphery especially near the corners along the void ceiling or floor. After the streamer occurs, it causes the local E-field distribution to be much different than the purely geometric E-field distribution. These differences mitigate or even prevent other streamers in the nearby region [14]. As the streamer develops, it erodes the overlapping regions of the top and bottom PFA layers. Due to the relatively high voltage excitation, the original E-field strength near the center of the void can be as high as 10.5 kV/mm before the streamer initiation. After the streamer initiation, the E-field strength near the center of the void will be lower but could still be higher than the breakdown strength of the air, which is about 3 kV/mm under a standard air condition. Thus, streamer and related erosion can still occur near the center of the void but should not be as severe as the regions at the void periphery. After PD aging, the erosion patterns in the overlapping regions of the top or bottom PFA layers near voids with varied diameters in the middle layer are shown in Fig.14. In Fig.14, the erosion does affect the edge geometry, but as the analysis predicts, there is little or no erosion at the void center compared with the erosion at the void periphery. Due to the non-equal erosion speed of the streamers, this correlation between the streamer initiation and the geometry of the aged polymer is shown in Fig. 15. Thus, the theoretical behavior matches the observed erosion patterns from the experiments. Moreover, significant material removal, which is perpendicular to the E-field and along the PFA layer interfaces, can be identified in voids with smaller diameters like 150 μm and 100 μm. This suggests that in the smaller volume voids, gas pressure and temperature effects are more significant than in the larger ones. However, even in the cases with void diameters of 150 μm or 100 μm, the remnants of the less eroded central region remain, as shown in Fig. 14 (c) and (d), which match the predictions from the E-field distribution analysis.

VII. CONCLUSION

The three-layer sample, consisting of three layers of polymer sheet with a cylindrical void in the central layer, serves as a useful surrogate to investigate the role of voids in the PD aging of cables for decades. The approach has been limited to larger diameter voids because of the mechanical nature of void production.

Laser drilling now makes it possible to explore the void-size space between the voids from 1000's of micrometers in radius used in the past to radii of a few micrometers which is typical of naturally occurring cable voids.

This investigation noted the influence of liquid formation, due to the effects of temperature and gas pressure. The primary conclusion, however, is that as the void volume changes by orders of magnitude, there is a dependence of the electric field distribution on the size and shape of the void.

In this paper, PD-erosion patterns observed from simulation analysis and experiments show that for the smaller laser-drilled voids, the electric field distribution drives the partial discharge activity away from the center of the void to the void periphery. This leads to a different erosion pattern in smaller voids than larger ones. Since there is a little or no erosion at the void center compared with the erosion at the void periphery, the experimental erosion patterns support the fact that streamer initiation in these laser-drilled small voids should appear at the void periphery especially near the corners of void ceiling or floor, as predicted by the simulation analysis. This may lead to a quite different aging speed and lifetime estimation compared with the data captured by using large mechanically drilled voids, which are widely used in the past to estimate the insulation lifetime under internal PD activities.

APPENDIX A
BOUNDARY ELEMENT ANALYSIS METHOD (BEM)

The objective of the boundary element formulation used by this team is encapsulated in Fig.16. Each dielectric object is replaced with a layer of surface charge on the interfacial skin. The fictitious layer of surface charge σ_1 on the interfacial layer of the body will serve to represent the body's induced field signature interior and exterior to the body. Since this method does not involve discretizing the surrounding volume, the accuracy of the method can be increased simply by increasing the number of unknowns on the interface [15]. The best analysis techniques involve assigning a high element weighting to the interface regions where the accuracy is most desired. In this work the regions involving corners are weighted 40 times heavier than those near open regions.

The layer of surface charge resides on the interface between the two dielectric materials. The surface charges are chosen to guarantee that the jump in tangential E-field is

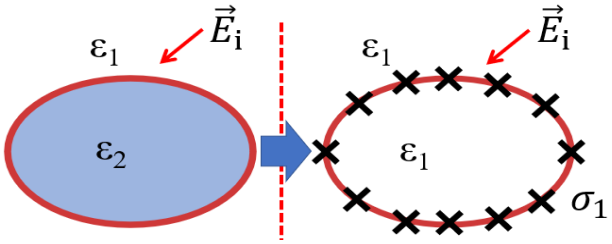

FIGURE 16. The objective of BEM used here is to replace the interface between two dielectric materials with a single surface layer charge σ_1.

continuous and the normal jump in the displacement field equals the enclosed surface charge, which can be found in (1) and (2) respectively. At this stage, we assume there is no free volume charge, ρ_f, only free surface charge, σ_f.

$$\hat{n} \times \left\| \vec{E} \right\| = 0 \tag{1}$$

$$\hat{n} \cdot \left\| \vec{D} \right\| = \sigma_f \tag{2}$$

where σ_f is the surface charge. $\vec{E}$ is the E-field vector and $\vec{D}$ is the displacement field vector.

The E-field is represented as the gradient of a scalar field Φ. Within the interior or exterior region, it follows that:

$$\nabla \cdot \varepsilon \vec{E} = \rho_f \tag{3}$$

Since the dielectric constant ε is piecewisecontinuous, it follows that:

$$\nabla^2 \Phi = \frac{\rho_f}{\varepsilon} = 0 \tag{4}$$

This equation is commonly represented in terms of finite elements or finite difference forms, but it can also be represented by an integral formulation via using Green's functions [16]. Green's theorem allows this to be written as:

$$\iiint_V \left\{ \Phi \nabla^2 G(r, r') - G(r, r') \nabla^2 \Phi \right\} dV = \iint_S \left\{ \Phi \frac{\partial G(r, r')}{\partial n} - G(r, r') \frac{\partial \Phi}{\partial n} \right\} dS \tag{5}$$

The free space Green's function in two dimensions is shown in (6),

$$G\left(r, r'\right) \frac{1}{2\pi \left| r - r' \right|}, \quad \text{Satisfying} -\nabla^2 G\left(r, r'\right) = 2\pi \delta \left(r - r'\right) \tag{6}$$

where δ is the Dirac delta function defined for the surface integral.

$$\iint_S \left\{ \Phi \frac{\partial G(r, r')}{\partial n} - G(r, r') \frac{\partial \Phi}{\partial n} \right\} dS' = \begin{cases} -2\pi \Phi\left(r\right) & r \in S \\ 0 & r \in V \end{cases} \tag{7}$$

The free surface charge σ_f at an interface can be written in terms of the electric field potential:

$$\sigma_{/\varepsilon} = {}^{\partial \Phi}/_{\partial n} \tag{8}$$

The simple layer formulation of Laplace's equation follows:

$$\iint_S G\left(r, r'\right) \sigma\left(r'\right) dS' = \varepsilon \Phi\left(r\right) \tag{9}$$

Application of the Neumann condition at the boundary for the surface charge in (2), a final equation for the surface charge can be achieved. By using $\Phi(r)$ and $G(r, r)$ to represent the normal derivatives of potential and Green's function with respect to the unprimedvariable, the final condition for the surface charge results:

$$\left(\varepsilon_1 - \varepsilon_2\right) \cdot \iint_S G'\left(r, r'\right) \sigma\left(r'\right) dS' + \left(\varepsilon_1 + \varepsilon_2\right) \sigma\left(r\right) = 0 \tag{10}$$

In the presence of an incident electric field, (10) becomes:

$$\left(\varepsilon_1 - \varepsilon_2\right) \cdot \iint_S G'^{(r,r')} \sigma\left(r'\right) dS' + \left(\varepsilon_1 + \varepsilon_2\right) \sigma\left(r\right) = \left(\varepsilon_1 - \varepsilon_2\right) \hat{n} \cdot \vec{E}_{inc} \tag{11}$$

Once this charge is found, the E-field at any point is the impressed E-field added to the Biot-Savart contribution from the charges of the dielectric interface. This field pattern is best computed by the integration of (9). A good seminal work outlining this type of integral analysis can be found in [17]. The solution of (11) is found by assuming a charge distribution along the interface. It can be piecewise constant, linear, or quadratic. In this work, Galerkin methods are used to solve these unknowns [18], [19].

APPENDIX B
OPTICAL INTERFEROMETRY, FOURIER TRANSFORM INFRARED SPECTROSCOPY, AND DIGITAL MICROSCOPE EQUIPMENT

Fourier Transform Infrared Spectroscopy (FTIR) was used to analyze the surface chemistry of the samples as shown in Fig. 6. FTIR is based around an optical microscope and uses an infrared light source to probe the chemical bonds in a material. Chemical bonds vibrate at characteristic frequencies and can absorb infrared frequencies, but only those frequencies that match their vibration modes. Measuring the radiation absorption as a function of frequency produces a spectrum that can be used to identify functional groups and compounds. Fig. 17 (a) shows the FTIR system we use. This system contains a fully automated microscope with video viewing.

Optical Interferometry (White Light Interferometry - WLI) is applied to capture the results as shown in Fig.15. The system, as shown in Fig.17 (b), was used to measure the surface topography of the samples. The instrument can achieve resolution height steps as small as 1×10^{-10} meter and the lateral resolution is limited to about 1×10^{-6} meter. The system can give magnification from 25x up to 1000x. The optical interferometry is an optical microscope-based technique used to measure the topography of surfaces. The technique utilizes the effect of constructive and destructive

interference of light. This interference is accomplished by splitting the source light into two paths. One path travels a fixed distance to mirror and is then reflected to the camera. The other path travels through a microscope objective lens, to the surface of interest and then reflects to the camera. The two light paths combine at the camera and the variation in distance travelled will result in an interference pattern at the camera. The measurement of topography occurs when the system slowly varies the distance of the objective from the surface of interest and tracks the changes in the interference pattern that result. A three-dimensional plot of the surface is then rendered from the data.

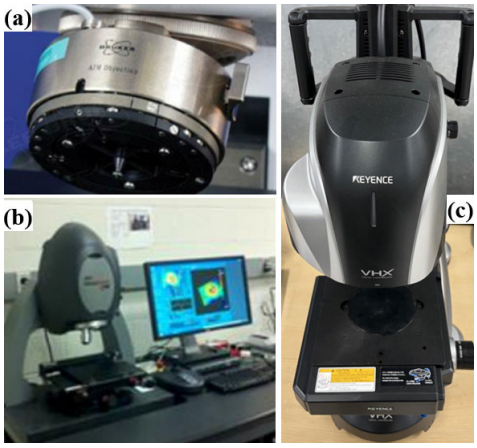

FIGURE 17. (a) FTIR instrument (b) Optical interferometry instrument (c) Digital microscope instrument.

The system as shown in Fig.1 (c), was used to check the size and shape of the laser drilled holes. This is a fully automated digital microscope system and has seamless transition in magnification from 20x to 6000x. Usually, the magnification of ∼1000x is sufficient to capture the details of the laser drilled hole with diameter of several tens of micrometers and typical results are provided in Fig.14.

ACKNOWLEDGMENT

The authors would like to thank Daniel Goberman, Anthony Ventura, and Gary Lomasney from the Raytheon Technology Research Center (RTRC) Measurement Sciences for their help with the material characterization.

Additional thanks go to Jonathan Hahne, John Nodler, Bruce Morrison, Bryan Bunkowski, and Claude Pullen from the Center for Electromechanics (CEM), The University of Texas at Austin, for their help with the test setup construction.

Finally, they also would like to acknowledge the contribution of Dr. Xianyong Feng. His initial guidance helped set the investigation on a technically productive path.

REFERENCES

[1] J. Li, W. Si, X. Yao, and Y. Li, "Measurement and simulation of partial discharge in oil impregnated pressboard with an electrical aging process," *Meas. Sci. Technol.*, vol. 20, no. 10, Sep. 2009, Art. no. 105701.

[2] L. Wang, A. Cavallini, G. C. Montanari, and L. Testa, "Evolution of PD patterns in polyethylene insulation cavities under AC voltage," *IEEE Trans. Dielectr. Electr. Insul.*, vol. 19, no. 2, pp. 533–542, Apr. 2012.

[3] X. Feng, Q. Xiong, A. L. Gattozzi, and R. E. Hebner, "Partial discharge experimental study for medium voltage DC cables," *IEEE Trans. Power Del.*, vol. 36, no. 2, pp. 1128–1136, Apr. 2021.

[4] M. Florkowski, B. Florkowska, M. Kuniewski, and P. Zydron, "Mapping of discharge channels in void creating effective partial discharge area," *IEEE Trans. Dielectr. Electr. Insul.*, vol. 25, no. 6, pp. 2220–2228, Dec. 2018.

[5] H. A. Illias, M. A. Tunio, A. H. A. Bakar, H. Mokhlis, and G. Chen, "Partial discharge phenomena within an artificial void in cable insulation geometry: Experimental validation and simulation," *IEEE Trans. Dielectr. Electr. Insul.*, vol. 23, no. 1, pp. 451–459, Feb. 2016.

[6] V. Madonna, P. Giangrande, and M. Galea, "Electrical power generation in aircraft: Review, challenges, and opportunities," *IEEE Trans. Transport. Electrific.*, vol. 4, no. 3, pp. 646–659, Sep. 2018.

[7] T. Ericsen and A. Tucker, "Power electronics building blocks and potential power modulator applications," in *Proc. Conf. Rec. 23rd Int. Power Modulator Symp.*, 1998, pp. 12–15.

[8] Y. Xu, X. Feng, J. Wang, C. Gao, R. Burgos, D. Boroyevich, and R. E. Hebner, "Medium-voltage SiC-based converter laminated bus insulation design and assessment," *IEEE J. Emerg. Sel. Topics Power Electron.*, vol. 7, no. 3, pp. 1715–1726, Sep. 2019.

[9] Y. Xu, J. Stewart, H. Song, L. Cheng, I. Cvetkovic, R. Burgos, and D. Boroyevich, "High power density medium-voltage converter integration via electric field management," *IEEE J. Emerg. Sel. Topics Power Electron.*, vol. 10, no. 1, pp. 895–905, Feb. 2022.

[10] L. R. Devi, A. Kumar Das, and S. Chatterjee, "Parameter analysis of power cable due to presence of void," in *Proc. IEEE 4th Int. Conf. Condition Assessment Techn. Electr. Syst. (CATCON)*, Nov. 2019, pp. 1–5.

[11] P. H. F. Morshuis, "Degradation of solid dielectrics due to internal partial discharge: Some thoughts on progress made and where to go now," *IEEE Trans. Dielectr. Electr. Insul.*, vol. 12, no. 5, pp. 905–913, Oct. 2005.

[12] K. Temmen, "Evaluation of surface changes in flat cavities due to ageing by means of phase-angle resolved partial discharge measurement," *J. Phys. D, Appl. Phys.*, vol. 33, no. 6, pp. 603–608, Mar. 2000.

[13] L. Niemeyer, "A generalized approach to partial discharge modeling," *IEEE Trans. Dielectr. Electr. Insul.*, vol. 2, no. 4, pp. 510–528, Aug. 1995.

[14] B. T. Murphy, R. E. Hebner, and E. F. Kelley, "Simulating mode transitions during breakdown in liquids," *IEEE Transactions Dielectr. Electrical Insulation*, vol. 18, no. 3, pp. 682–691, Jun. 30, 2011.

[15] R. F. Harrington, K. Pontoppidan, P. Abrahamsen, and N. C. Albertsen, "Computation of Laplacian potentials by an equivalent source method," *Proc. IEE*, vol. 166, no. 10, pp. 1715–1720, Oct. 1969.

[16] J. A. Stratton, *Electromagnetic Theory*. New York, NY, USA: McGraw-Hill, 1941, pp. 163–167.

[17] Y. B. Yildir, K. M. Prasad, and D. Zheng, "Computer aided design in electromagnetic systems: Boundary element method and applications," *Control Dyn. Syst.*, vol. 59, pp. 167–223, Aug. 1993.

[18] Y. G. Smirnov and A. A. Tsupak, "Galerkin method for solving of singular integral equation of diffraction problem," in *Proc. Int. Conf. Math. Methods Electromagn. Theory*, 2002, pp. 1–15.

[19] K. R. Davey and D. Zheng, "Error tracking in boundary element formulations," *IEEE Trans. Magn.*, vol. 32, no. 1, pp. 259–264, Jan. 1996.

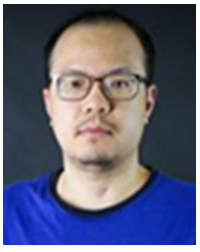

YUE XU (Member, IEEE) received the B.S. degree in electrical engineering from Xi'an Jiaotong University, Xi'an, China, in 2012, the M.S. degree in electrical engineering from Illinois Institute of Technology, Chicago, IL, USA, in 2015, and the Ph.D. degree in electrical engineering from Virginia Polytechnic Institute and State University, Blacksburg, VA, USA, in 2021. He is currently a Postdoctoral Fellow with the Center for Electromechanics (CEM), The University of Texas at Austin, Austin, TX, USA. He conducts insulation material development and testing for power applications as well. His research interests include insulation design, offline assessment, and online monitoring for medium/high voltage and high-power density power electronics equipment.

KENT DAVEY (Life Fellow, IEEE) received the B.S. degree in electrical engineering from Tulane University, in 1974, the M.S. degree in power engineering from Carnegie Mellon University, in 1976, the M.S. degree in physics from the University of Pittsburgh, and the Ph.D. degree in electrical engineering from MIT, in 1979. He is currently a Senior Research Fellow with the Center for Electromechanics, The University of Texas at Austin, Austin, TX, USA. He is an Editor of IEEE TRANSACTIONS ON MAGNETICS.

WENPING ZHAO received the B.S. degree in mechanical engineering from Tsinghua University, Beijing, China, in 1991, and the Ph.D. degree in mechanical engineering from Purdue University, West Lafayette, IN, USA, in 1999. He is currently the Associate Director of advanced materials and mechanics of the RTX Research Center. His research interests include polymers, polymer matrix composites and their wide spectrum of applications in aerospace, defense, and other industries.

ROBERT E. HEBNER (Life Fellow, IEEE) received the B.S. degree in physics from Saint Mary's University, San Antonio, TX, USA, in 1967, and the M.S. and Ph.D. degrees in physics from the University of Missouri, Rolla, MO, USA, in 1969 and 1971, respectively. After a long career with the National Institute of Standards and Technology, Gaithersburg, MD, USA, he accepted the position as the Director of the Center for Electromechanics, The University of Texas at Austin, Austin, TX, USA. His research interests include dielectrics and electrical insulation applications.

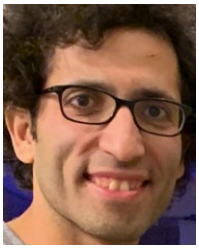

MIAD YAZDANI received the B.Sc. degree in mechanical engineering from the Sharif University of Technology, Tehran, Iran, in 2004, and the M.Sc. and Ph.D. degrees in mechanical engineering from Illinois Institute of Technology, Chicago, IL, USA, in 2005 and 2009, respectively. His research interests include the enhancement of heat transfer and mass transport control with electrohydrodynamics in macro- and microscale systems.